Supplementary Information for:

Accelerating Solid-State Battery Design: Predicting Ionic Conductivity with Machine Learning Potentials

Ailian Wang[a], Xiaoyan Fu[a*], Panfeng Ji[a], Jinzhe Ma[a], Zhongwei Zhang[a], P. Hu[a,b*]

[a] School of Physical Science and Technology, ShanghaiTech University, Shanghai 201210, China

[b] School of Chemistry and Chemical Engineering, The Queen's University of Belfast, Belfast BT9 5AG, UK

To further support the main text's investigation of lithium-ion diffusion behavior in typical sulfide-based solid-state electrolytes, this section systematically presents the basic structural information and molecular dynamics simulation results of eight representative materials. The selected materials include Li_3PS_4, Li_7PS_6, $Li_7P_3S_{11}$, $Li_{48}P_{16}S_{61}$, Li_4GeS_4, Li_4SnS_4, $Li_{10}Ge(PS_6)_2$, $Li_{10}Sn(PS_6)_2$. All structures were obtained from the Materials Project database and have been optimized using first-principles calculations, ensuring good crystallographic stability and reference experimental performance.

Table S1. Properties of Li-Ion Solid-State Electrolytes from the Materials Project

Chemical Formula	Materials ID	Crystal System	Space Group	Volume (Å^3)	Number of Li^+	Band Gap(eV)
Li_3PS_4	mp-1097036	Orthorhombic	Pnma	641.38	12	2.48
Li_7PS_6	mp-1211324	Orthorhombic	Pna2_1	1001.83	28	2.08
$Li_7P_3S_{11}$	mp-641703	Triclinic	$P\bar{1}$	876.77	14	2.49
$Li_{48}P_{16}S_{61}$	mp-1001069	Monoclinic	P1m1	2652.95	48	2.30
Li_4GeS_4	mp-1222582	Orthorhombic	Pna2_1	683.08	16	2.51

Li_4SnS_4	mp-1195718	Orthorhombic	Pnma	709.34	16	2.36
$Li_{10}Ge(PS_6)_2$	mp-696128	Tetragonal	$P4_2mc$	977.45	20	2.33
$Li_{10}Sn(PS_6)_2$	mp-696123	Tetragonal	$P4_2mc$	1007.51	20	2.27

In this study, each material was expanded into a 2×2×2 supercell and subjected to molecular dynamics simulations using the trained machine learning potential at temperatures ranging from 600 K to 1000 K. The simulation trajectories were used to calculate the time-dependent mean squared displacement (MSD) of Li^+ ions, providing insight into the diffusion behavior and its thermal dependence.

Through this comprehensive analysis, the trained potential is further validated across various structural frameworks and temperature conditions, demonstrating both its transferability and reliability. These results also offer valuable data for understanding the diffusion mechanisms of different types of solid electrolytes under realistic operating conditions. The corresponding MSD plots and Arrhenius plots of ln(D) versus 1/T are presented below, offering direct evidence of the temperature-dependent ionic transport behavior.

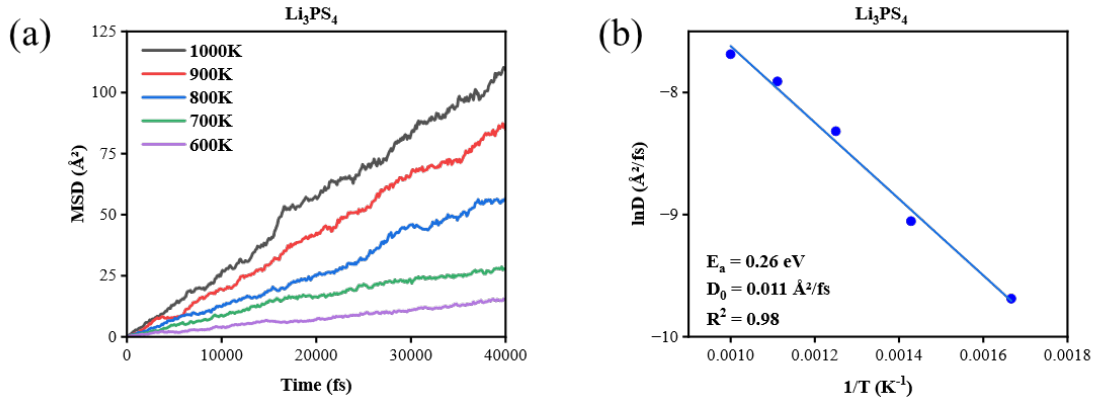

Figure S1. (a) Li-ion MSD curves at different temperature in Li_3PS_4. (b) Arrhenius plots (ln(D) vs. 1/T) for Li_3PS_4.

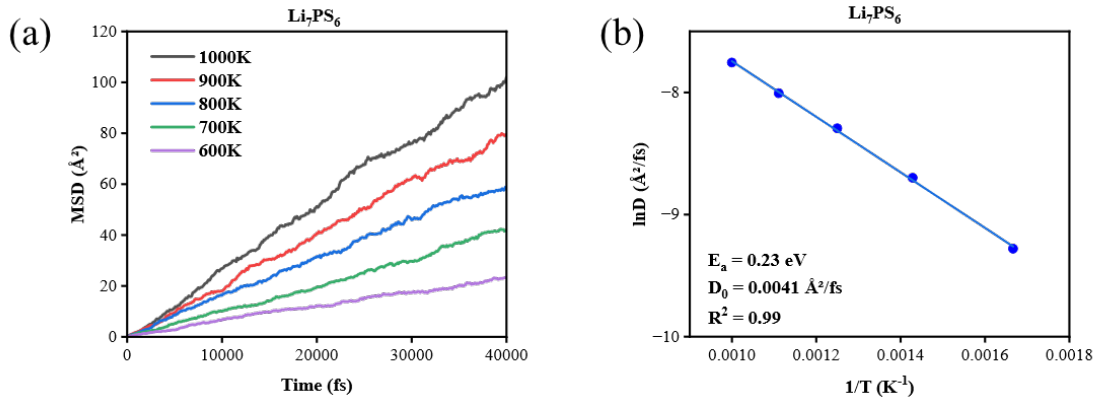

Figure S2. (a) Li-ion MSD curves at different temperature in Li_7PS_6. (b) Arrhenius plots (ln(D) vs. 1/T) for Li_7PS_6.

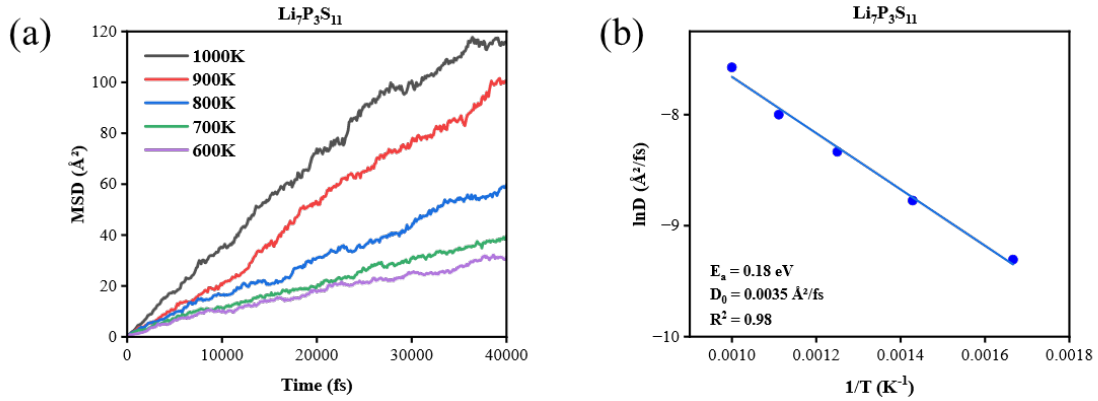

Figure S3. (a) Li-ion MSD curves at different temperature in $Li_7P_3S_{11}$. (b) Arrhenius plots (ln(D) vs. 1/T) for $Li_7P_3S_{11}$.

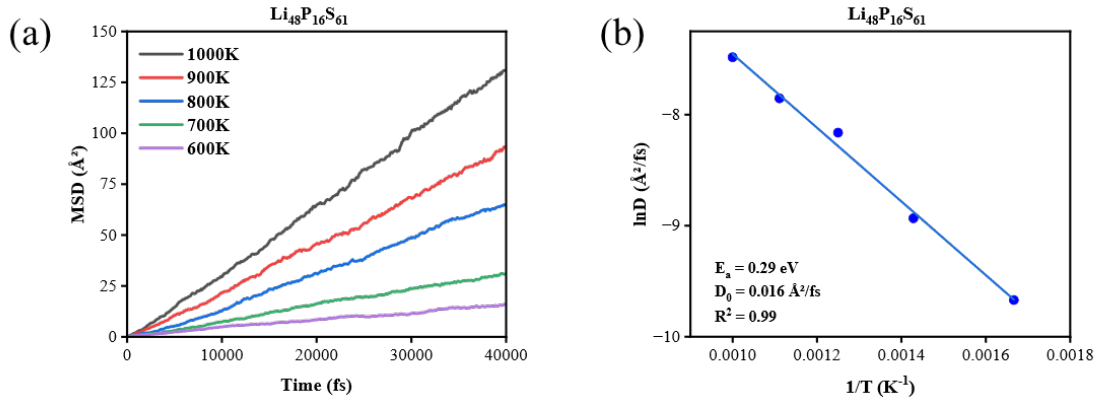

Figure S4. (a) Li-ion MSD curves at different temperature in $Li_{48}P_{16}S_{61}$. (b) Arrhenius plots (ln(D) vs. 1/T) for $Li_{48}P_{16}S_{61}$.

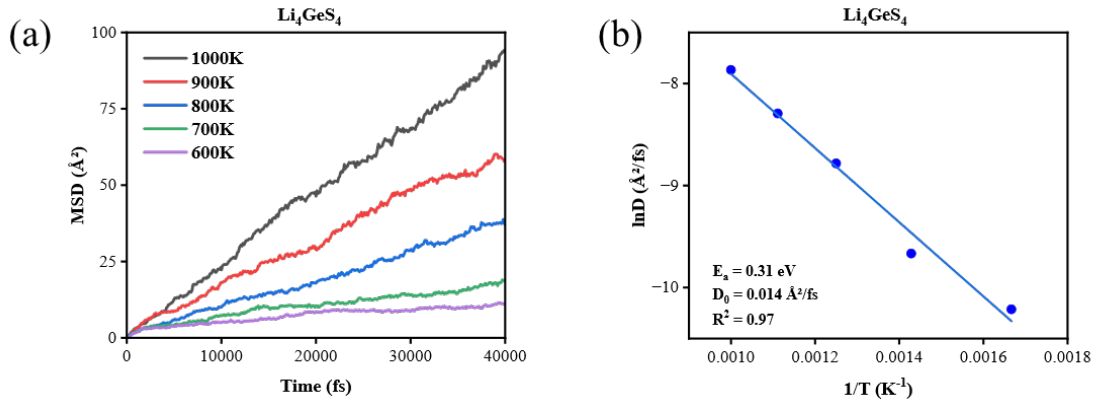

Figure S5. (a) Li-ion MSD curves at different temperature in Li_4GeS_4. (b) Arrhenius plots (ln(D) vs. 1/T) for Li_4GeS_4.

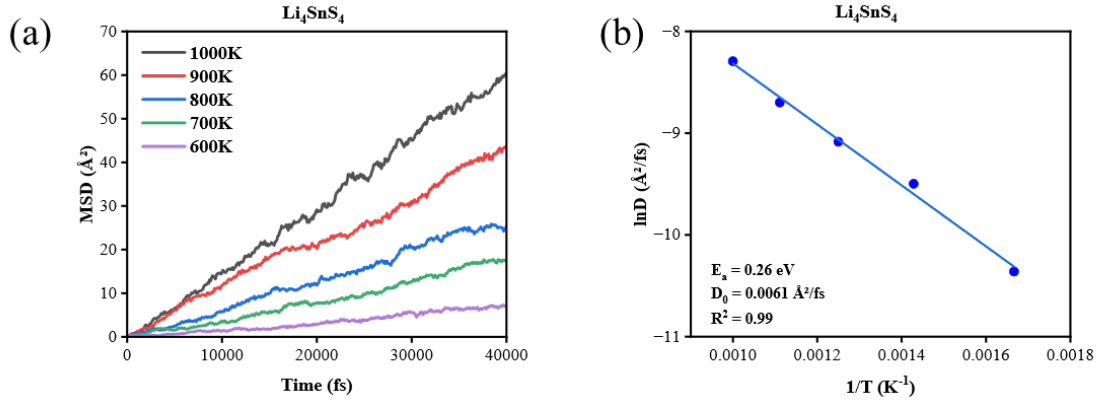

Figure S6. (a) Li-ion MSD curves at different temperature in Li_4SnS_4. (b) Arrhenius plots (ln(D) vs. 1/T) for Li_4SnS_4.

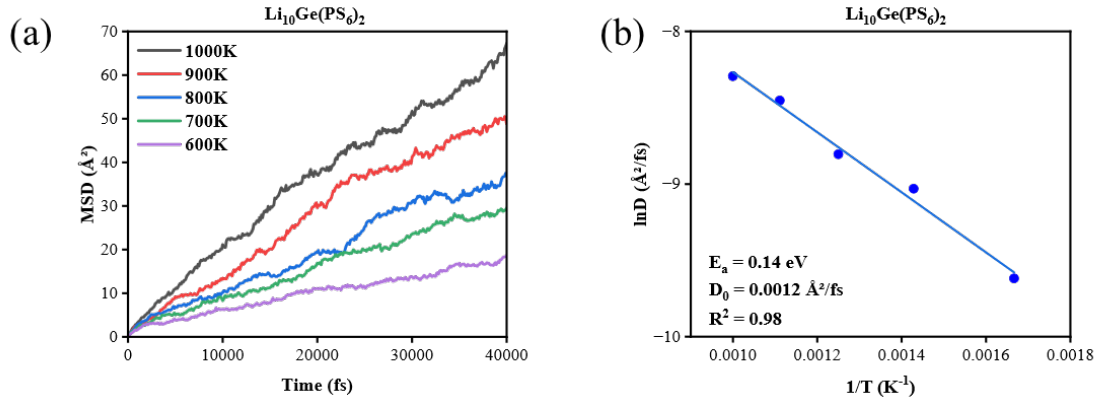

Figure S7. (a) Li-ion MSD curves at different temperature in $Li_{10}Ge(PS_6)_2$. (b) Arrhenius plots (ln(D) vs. 1/T) for $Li_{10}Ge(PS_6)_2$.

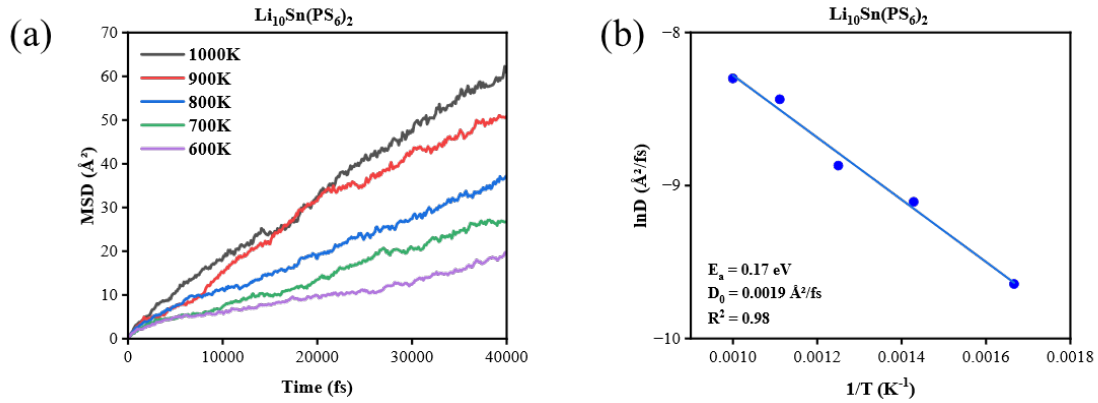

Figure S8. (a) Li-ion MSD curves at different temperature in $Li_{10}Sn(PS_6)_2$. (b) Arrhenius plots (ln(D) vs. 1/T) for $Li_{10}Sn(PS_6)_2$.

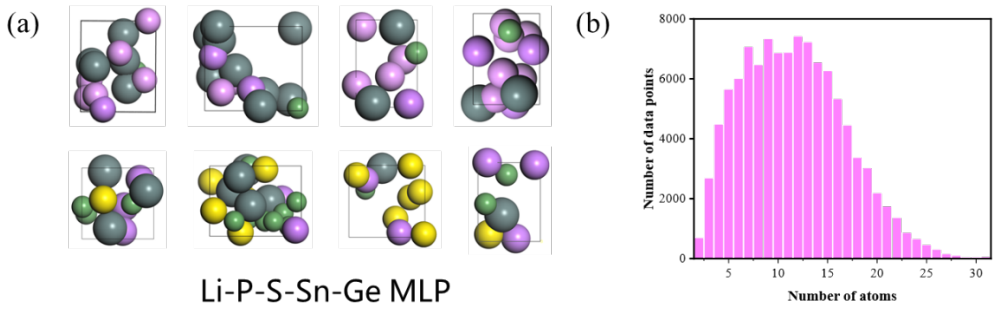

Figure S9. (a) Representative structures of the training dataset. The structures were generated with random lattice parameter, random atomic composition and random atomic position. (b) The statistical counts of structures across different atomic numbers, visualized in a histogram.

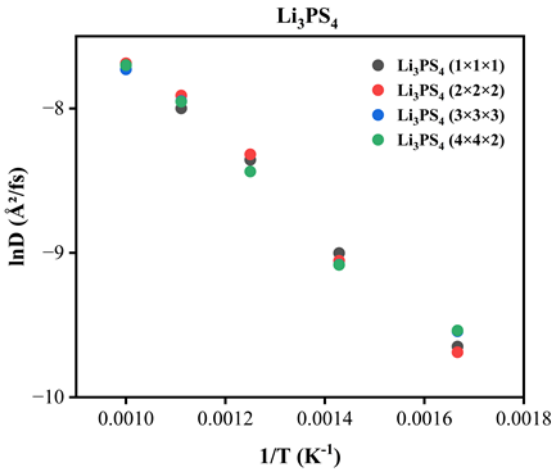

Figure S10. Arrhenius plots (ln(D) vs. 1/T) for Li_3PS_4 with different supercells:

(1×1×1), (2×2×2), (3×3×3), and (4×4×2). It is clear that the differences in diffusion coefficients among these supercells are not significant, indicating that the supercell size has negligible impact on the Li-ion diffusion behavior in Li_3PS_4 within the investigated range.

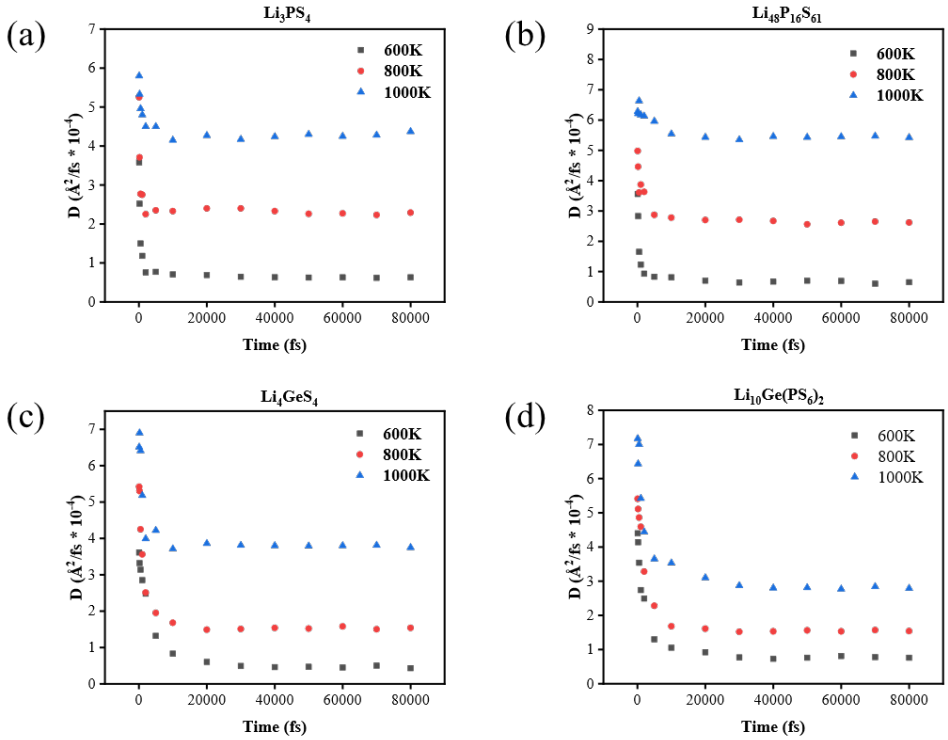

Figure S11. Convergence tests of the calculated diffusion coefficient at 600 K, 800 K, and 1000 K as a function of MD simulation duration for different structures: (a) Li_3PS_4, (b) $Li_{48}P_{16}S_{61}$, (c) Li_4GeS_4, and (d) $Li_{10}Ge(PS_6)_2$. These plots demonstrate that the diffusion coefficients converge within 80 ps of MD simulation across different investigated structures, supporting the choice of a 40 ps MD simulation duration for reliable diffusion coefficient calculations.

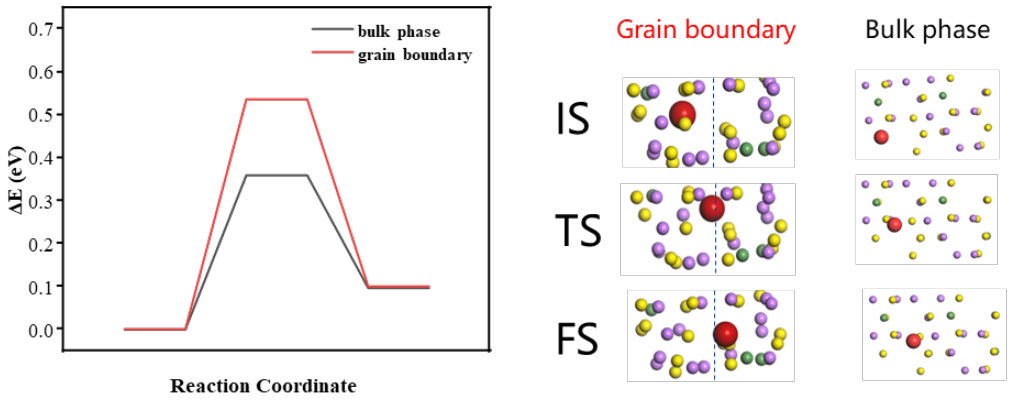

Figure S12. Comparison of relative energy of Li^+ migration in the bulk phase and (111)/(110) grain boundary of Li_4GeS_4 as a function of the reaction coordinate. The structural schematics illustrate the initial state, transition state, and final state of Li^+ migration. The red sphere represents the migrating Li^+; purple spheres denote Ge atoms, yellow spheres denote S atoms, and green spheres denote other Li atoms in the local environment.

Table S2. Surface energies of Li, Sn, and Ge with (111), (110), and (100) crystal facets calculated by DFT and MLP (Unit: eV/Å²). They show that the MLP results are very similar to those from DFT calculations.

	Li (111)	Li (110)	Li (100)	Sn (111)	Sn (110)	Sn (100)	Ge (111)	Ge (110)	Ge (100)
DFT	0.039	0.030	0.020	0.035	0.050	0.071	0.062	0.075	0.097
MLP	0.035	0.026	0.020	0.034	0.045	0.072	0.061	0.072	0.097

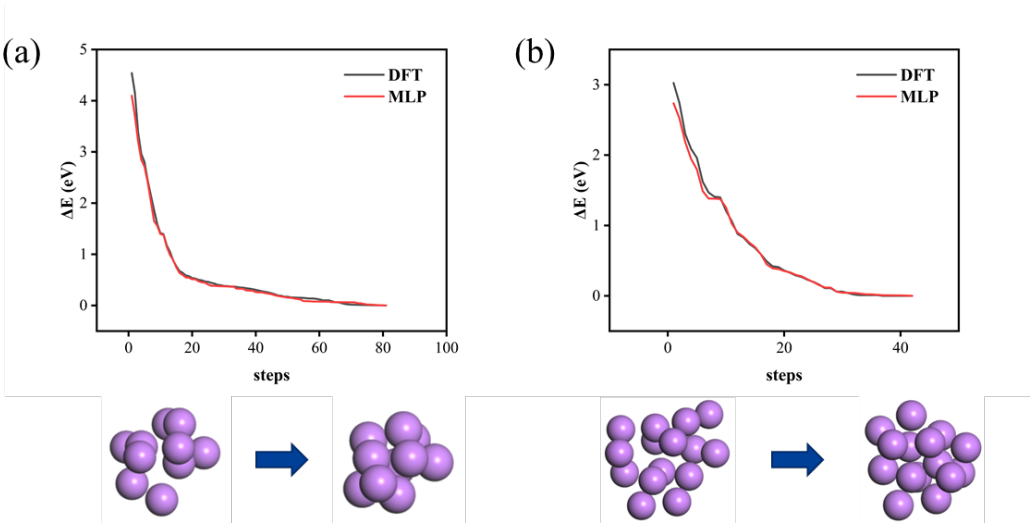

Figures S13. Generalization test via the relaxation of perturbed clusters. This figure shows the energy relaxation trajectories for two structures not included in the training set: (a) Li_{10} and (b) Li_{15}. In each case, the system was first displaced into an unstable state and then allowed to relax. The energy difference (ΔE) is measured relative to the fully relaxed state.

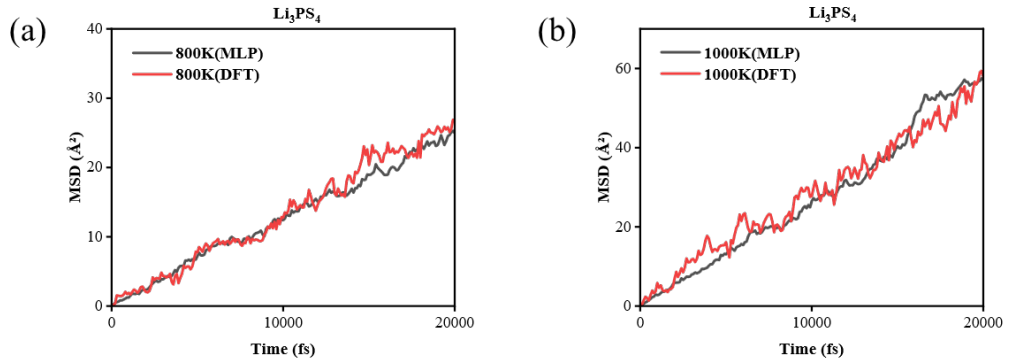

Figure S14. Comparison of mean squared displacement (MSD) from MLP (gray) and MD (red) at 800 K (a) and 1000 K (b). The MLP and MD results show consistent trends at both temperatures.

Table 3. Potentials corresponding to different decomposition products in atomic-substituted LGPS-based electrolytes (varied Ge/Sn ratios). We chose the most stable decomposition pathways, obtaining the narrowest electrochemical window.

Ge/Sn	Li_2S, Ge, Sn, P	P_2S_5, GeS_2, SnS_2, S	P, Li_4SnS_4, Li_4GeS_4, Li_2S	Li_3PS_4, GeS_2, SnS_2, S
	reduction potential (V)	oxidation potential (V)	reduction potential (V)	oxidation potential (V)
∞	1.54	2.15	1.61	2.03
15/1	1.54	2.15	1.62	2.01
7/1	1.54	2.16	1.62	2.02
3/1	1.54	2.17	1.62	2.03
1/1	1.55	2.17	1.63	2.04
1/3	1.55	2.18	1.63	2.04
1/7	1.55	2.19	1.63	2.06
1/15	1.54	2.19	1.63	2.07
0	1.53	2.20	1.62	2.08